Numerical Experiments on the Excitation and Propagation of Tsunamis Due to Air Pressure Waves over Seabed Topography

Taro Kakinuma[1)] and Jungo Kosugi[2)]

[1)] Graduate School of Science and Engineering, Kagoshima University
[2)] Civil Engineering Department, Kagoshima Prefectural Government

1. Introduction

Tsunamis were widely observed when the large eruption of Hunga Tonga–Hunga Ha`apai volcano occurred in January, 2022. After the eruption, the atmospheric Lamb wave with the largest pressure deviation of approximately 2 hPa was observed in Japan [1]. Therefore, one of the sources that caused the tsunamis observed far away from the eruption site was considered to be the Proudman resonance [2], which is also an origin of meteotsunamis, e.g., [3]. Regarding eruption tsunamis before this Tonga eruption, the 1883 Krakatau volcanic eruption tsunamis [4–12] and the 1956 Bezymianny volcanic eruption tsunamis [12, 13] have been studied.

The investigations on the 2022 Hunga Tonga–Hunga Ha`apai volcanic eruption tsunamis were started early after the event: for example, the relationship between the air pressure waves and resultant tsunamis was studied using numerical models [14, 15]. Thereafter, many papers have been published and the research on the Tonga eruption tsunamis continues: for example, numerical calculations using an ocean model with atmospheric models were performed to reproduce the sea level fluctuations along the Japanese coasts, resulting that the Proudman resonance due to the Pekeris waves [16] caused the significant tsunamis at Kushiro and Miyako in eastern Japan [17]. However, those at Tosashimizu and Kushimoto in western Japan could not be explained, and the amplification mechanism of tsunamis with a total amplitude of more than 2 m, which was observed at Amami in southern Japan [1], is also still unknown. Furthermore, although tsunamis due to air pressure waves were calculated considering seabed topographies [8, 14, 18, 19], there are many aspects that remain unclear especially regarding the effect of air pressure waves on air-sea waves propagating over seabed topographies.

In the present study, as a fundamental investigation on air-sea waves, numerical experiments were generated to study tsunamis propagating over typical seabed topographies while being influenced by steady air pressure waves traveling at a constant velocity, using a nonlinear shallow water model on velocity potential of tsunamis.

2. Numerical method and conditions

2.1. Numerical method

We consider the irrotational motion of an inviscid and incompressible fluid. When considering the pressure $p(\boldsymbol{x}, t)$ at the water surface, the nonlinear shallow water equations on velocity potential $\phi(\boldsymbol{x}, t)$ are described as

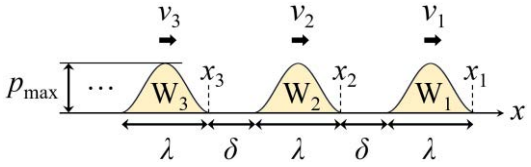

Figure 1. Wave profiles of steady air pressure waves traveling in the positive direction of the x-axis at the initial time, namely $t = 0$ s, where the interval between the waves is δ and the location of the onshore end of the nth wave W_n is x_n. The wavelength, maximum air pressure, and traveling velocity of W_n are denoted by λ, $p_{\max}$, and v_n, respectively.

$$\partial\eta/\partial t = -\nabla[(\eta - b)\nabla\phi], \tag{1}$$

$$\partial\phi/\partial t = -(\nabla\phi)^2/2 - g\eta - p/\rho, \tag{2}$$

where $\eta(\boldsymbol{x}, t)$ and $b(\boldsymbol{x})$ are water surface displacement and seabed position, respectively; ∇ is a horizontal partial differential operator $(\partial/\partial x, \partial/\partial y)$. The gravitational acceleration g is 9.8 m/s^2 and the sea water density ρ is 1030 kg/m^3.

In this study, we consider the one-dimensional propagation of waves along the x-axis direction. Equations (1) and (2) were solved numerically using a finite difference method with central and forward difference schemes for space and time, respectively. The grid size Δx and time step interval Δt were determined to be 500 m and 0.7 s, respectively, after accuracy verification. The initial value of velocity potential, $\phi(x, 0\text{ s})$, was 0 m^2/s at any location. The verification of the numerical model is discussed by comparing the numerical results of the maximum water surface displacement $\eta_{\max}$ with the corresponding linear theoretical solutions [3, 8].

2.2. Air pressure wave model

We introduced an air pressure wave model to represent the fundamental effects of air pressure waves on the generation and amplification processes of tsunamis. We assumed that the steady air pressure waves, as depicted in Figure 1, traveled onshore, i.e., in the positive direction of the x-axis. At the initial time, namely $t = 0$ s, the interval between the air pressure waves was δ, and the location of the onshore end of the nth air pressure wave W_n was x_n. The traveling velocity of W_n, namely v_n, is assumed to be constant.

The profile of the air pressure waves is a sinusoidal shape, which is described at the initial time as

$$p(x) = \frac{p_{\max}}{2}\left[1 - \sin\frac{2\pi}{\lambda}\left(x - x_n + \frac{5\lambda}{4}\right)\right], \quad x_n - \lambda \le x \le x_n, \quad t = 0\text{ s}. \tag{3}$$

When only one air pressure wave travels, its wave profile is illustrated in Figure 2, in which the traveling velocity of the air pressure wave is simply denoted by v. In the computation, the maximum air pressure $p_{\max}$ and wavelength λ were 2 hPa and 20 km, respectively, for any of the air pressure waves. Although it may be excessive to set the maximum air pressure to 2 hPa for air pressure waves due to an eruption other than atmospheric Lamb waves, it is a general value for air pressure fluctuations that generate

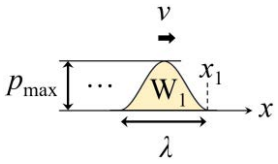

Figure 2. Wave profile of a steady air pressure wave W_1 traveling in the positive direction of the x-axis at the initial time, where the location of the onshore end of W_1 is x_1, in Cases 1–4. The wavelength, maximum air pressure, and traveling velocity of W_1 are denoted by λ, p_{max}, and v, respectively.

Table 1. Calculation conditions of the air pressure waves in Cases 1–6.

Case	Figure	x_1	x_2	x_3	v_1 or v	v_2	v_3
Case 1	Figure 2	35 km	—	—	250 m/s	—	—
Case 2					170 m/s		
Case 3							
Case 4					200 m/s		
Case 5	Figure 1	85 km	55 km	25 km	250 m/s	220 m/s	200 m/s
Case 6							

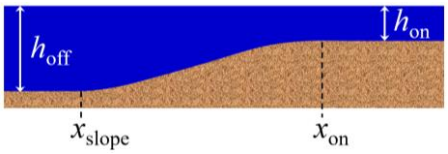

Figure 3. Seabed topography which includes a slope at $x_{slope} \le x \le x_{on}$ in Cases 1–3.

meteotsunamis. The calculation conditions of the air pressure waves are described in Table 1.

2.3. Seabed topographies

Figure 3 depicts a seabed topography including a slope, in the numerical experiments for Cases 1–3. The still water depth in the offshore deepest area is denoted by h_{off}, whereas that in the onshore shallowest area is h_{on}. The profile of the seabed slope is a sinusoidal shape and described by

$$b(x) = -h_{on} - \frac{h_{off} - h_{on}}{2}\left(1 + \cos\frac{x - x_{slope}}{x_{on} - x_{slope}}\pi\right), \quad x_{slope} \le x \le x_{on}. \tag{4}$$

The calculation conditions of the seabed topographies in Cases 1–3 are described in Table 2.

Conversely, Figure 4 presents two types of seabed topographies including multiple slopes. Figure 4(a) illustrates a seabed including four slopes, while Figure 4(b) includes three slopes. The former roughly models the seabed topography between Tonga and Amami Oshima Island, Kagoshima, Japan, while the latter imagines the area between Tonga and Chichijima Island, Tokyo, Japan. The calculation conditions of the seabed topographies in Cases 4–6 are described in Tables 3 and 4.

Table 2. Calculation conditions of the seabed topographies in Cases 1–3.

Case	Figure	x_{slope}	x_{on}	h_{off}	h_{on}
Case 1	Figure 3	150 km	550 km	4000 m	500 m
Case 2					
Case 3				3800 m	

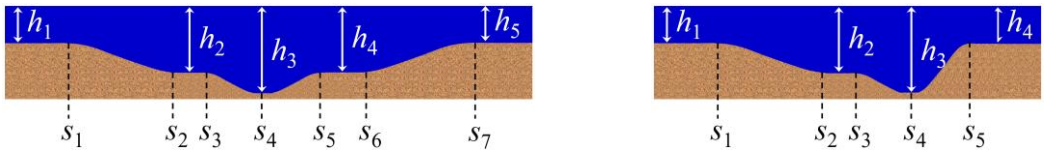

(a) Four-slope type in Cases 4 and 5 **(b)** Three-slope type in Case 6

Figure 4. Seabed topographies which include multiple slopes in Cases 4–6.

Table 3. Switching positions of the seabed slopes in Cases 4–6.

Case	Figure	s_1	s_2	s_3	s_4	s_5	s_6	s_7
Case 4	Figure 4(a)	100 km	200 km	300 km	400 km	500 km	600 km	700 km
Case 5								
Case 6	Figure 4(b)						—	—

Table 4. Still water depths in Cases 4–6.

Case	Figure	h_1	h_2	h_3	h_4	h_5
Case 4	Figure 4(a)	1500 m	4000 m	8000 m	4000 m	1500 m
Case 5						
Case 6	Figure 4(b)				1500 m	—

3. Generation and propagation of tsunamis due to an air pressure wave over a seabed including a slope

3.1. Case 1: $v > c$

In Case 1, an air pressure wave traveled over a seabed including a slope as illustrated in Figure 3. The calculation conditions are described in Tables 1 and 2. If a tsunami can be assumed to be a linear shallow water wave, the tsunami speed c is approximately $\sqrt{gh}$, where h is still water depth. In Case 1, c is approximately $\sqrt{gh_{\mathrm{off}}} \simeq 198$ m/s in the deepest area and the traveling velocity of the air pressure wave, v, is 250 m/s, so $v > c$ in the whole region. The time variations of both the air pressure and water surface displacement are presented in Figure 5, with the seabed profile. As depicted in Figure 5(a), a tsunami crest and trough are generated and amplified by the Proudman resonance in the deepest area, whereafter, as shown in Figures 5(b) and 5(c), the air pressure wave, accompanied by the tsunami crest,

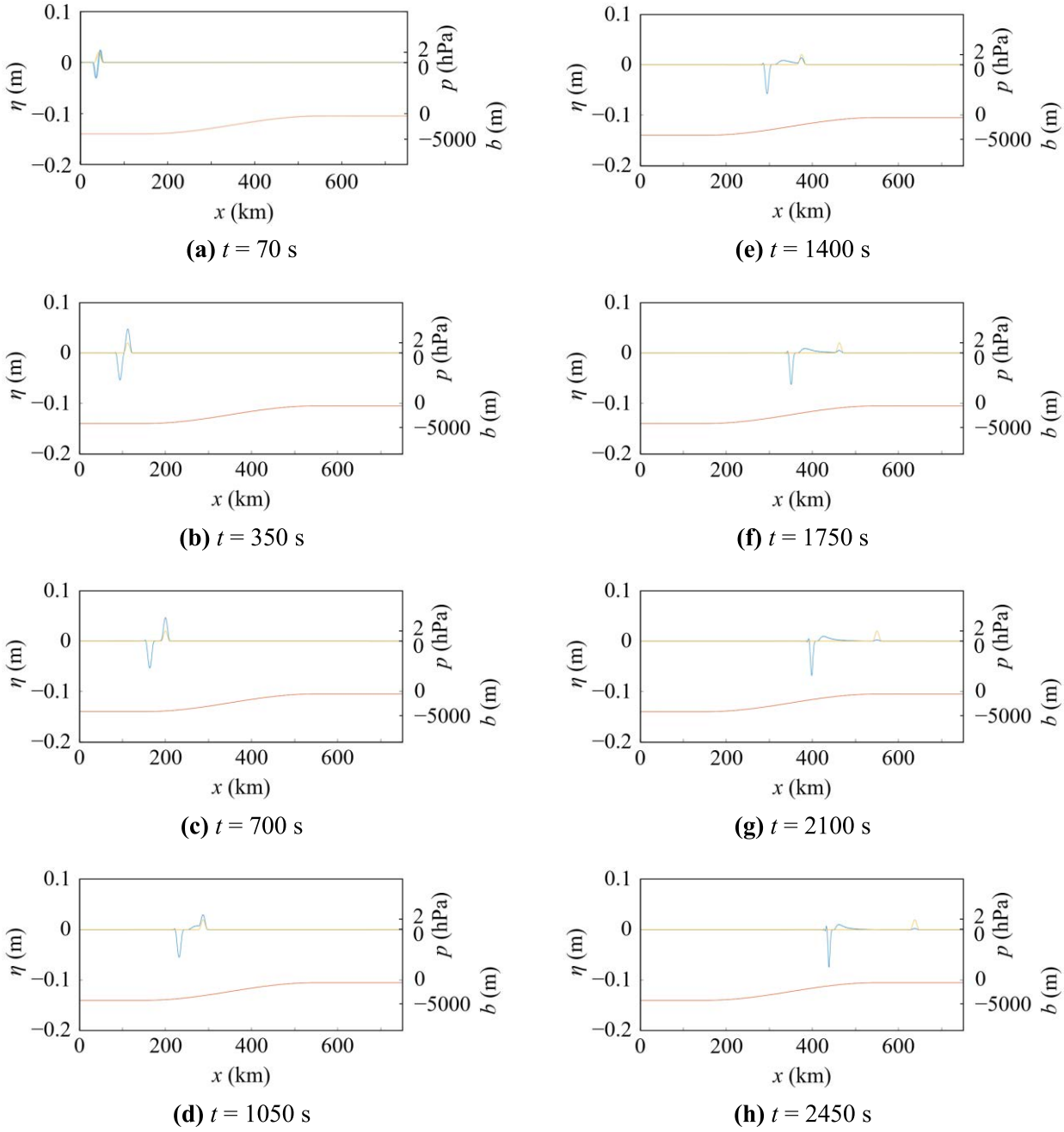

Figure 5. Time variations of the air pressure and water surface profiles in Case 1. The yellow, blue, and orange lines indicate the air pressure p, water surface displacement η, and seabed position b, respectively. The conditions are described in Tables 1 and 2.

precedes the tsunami trough.

Over the uphill slope, as depicted in Figures 5(d)–5(f), the tsunami height of the forced crest component following the air pressure wave is reduced, and the air pressure wave leaves a free crest component with a longer wavelength. The slope of the back of the newly built free crest is milder than the corresponding result in Figure 10 from [18], because the seabed slope is gradually change in the x-axis direction in the present case, while that is suddenly change at the slope end in [18]. In Figure 5(g),

the free tsunami crest which has been apart from the air pressure wave is amplified by shoaling, as described in [14] and [19], and so is the free tsunami trough. Figure 5(h) indicates, from the right, the forced tsunami crest that follows the air pressure wave, the free tsunami crest, and the free tsunami trough, propagating onshore.

3.2. Case 2: $v < c$ in the deepest area and $v > c$ in the shallowest area

In Case 2, an air pressure wave traveled over a seabed including a slope as illustrated in Figure 3, and the calculation conditions are described in Tables 1 and 2. In this case, the approximate value of tsunami speed, c, is $\sqrt{gh_{\text{off}}} \simeq 198$ m/s in the deepest area and $\sqrt{gh_{\text{on}}} = 70$ m/s in the shallowest area. Conversely, the traveling velocity of the air pressure wave, v, is 170 m/s, so $v < c$ in the deepest area, while $v > c$ in the shallowest area. The time variations of both the air pressure and water surface displacement are depicted in Figure 6, with the seabed profile. In the deepest area, although Figure 6(a) indicates that a tsunami crest and trough are generated and amplified as in Figure 5(a) for Case 1, the air pressure wave, accompanied by the tsunami trough, is preceded by the tsunami crest in Figures 6(b) and 6(c), unlike in Case 1. We call this free tsunami crest the first free tsunami crest.

Over the uphill slope, as depicted in Figure 6(d), the tsunami height of the first free tsunami crest increases by shoaling. In Figure 6(e), the air pressure wave generates a new tsunami crest through the Proudman resonance, because the traveling velocity of the air pressure wave, v, is 170 m/s and the resonance effect is maximized when the still water depth h is around 2950 m. The air pressure wave also excites a tsunami trough, and this trough overlaps the forced tsunami trough which has followed the air pressure wave, so the amplitude of the tsunami trough has become larger than that of the tsunami crest in the tsunami generation process. Thereafter, as shown in Figure 6(f), the tsunami trough is released from the restraint of the air pressure wave, and this free tsunami trough is amplified over the uphill slope with a wavelength that gradually becomes shorter. In Figure 6(g), the air pressure wave accompanied by a forced component of the new tsunami crest leaves a free component of the new tsunami crest. We call this free component of the new tsunami crest the second free tsunami crest. When the air pressure wave catches up with the first free tsunami crest, which has been amplified by shoaling, the tsunami height of the first free tsunami crest increases, because the forced component of the new tsunami crest following the air pressure wave overlaps the first free tsunami crest. It should be noted that after an air pressure wave passes a free tsunami crest, the tsunami height of the free tsunami crest returns to the value before being passed by the air pressure wave over a flat seabed, but the free tsunami crest obtains a larger tsunami height even after being passed by an air pressure wave over an upslope seabed [18]. This is because as the still water depth becomes shallower and the effect of the Proudman resonance decreases over an upslope seabed, the energy of the forced tsunami crest component following an air pressure wave decreases and the residual energy is added to the free tsunami crest being passed by the air pressure wave. In Figure 6(h), the first free tsunami crest, which are amplified by shoaling, has been further amplified by being passed by the air pressure wave, over the upslope seabed. This figure indicates, from the right, the forced tsunami crest that follows the air pressure wave, the first free tsunami crest, the second free tsunami crest, and the free tsunami trough propagating onshore.

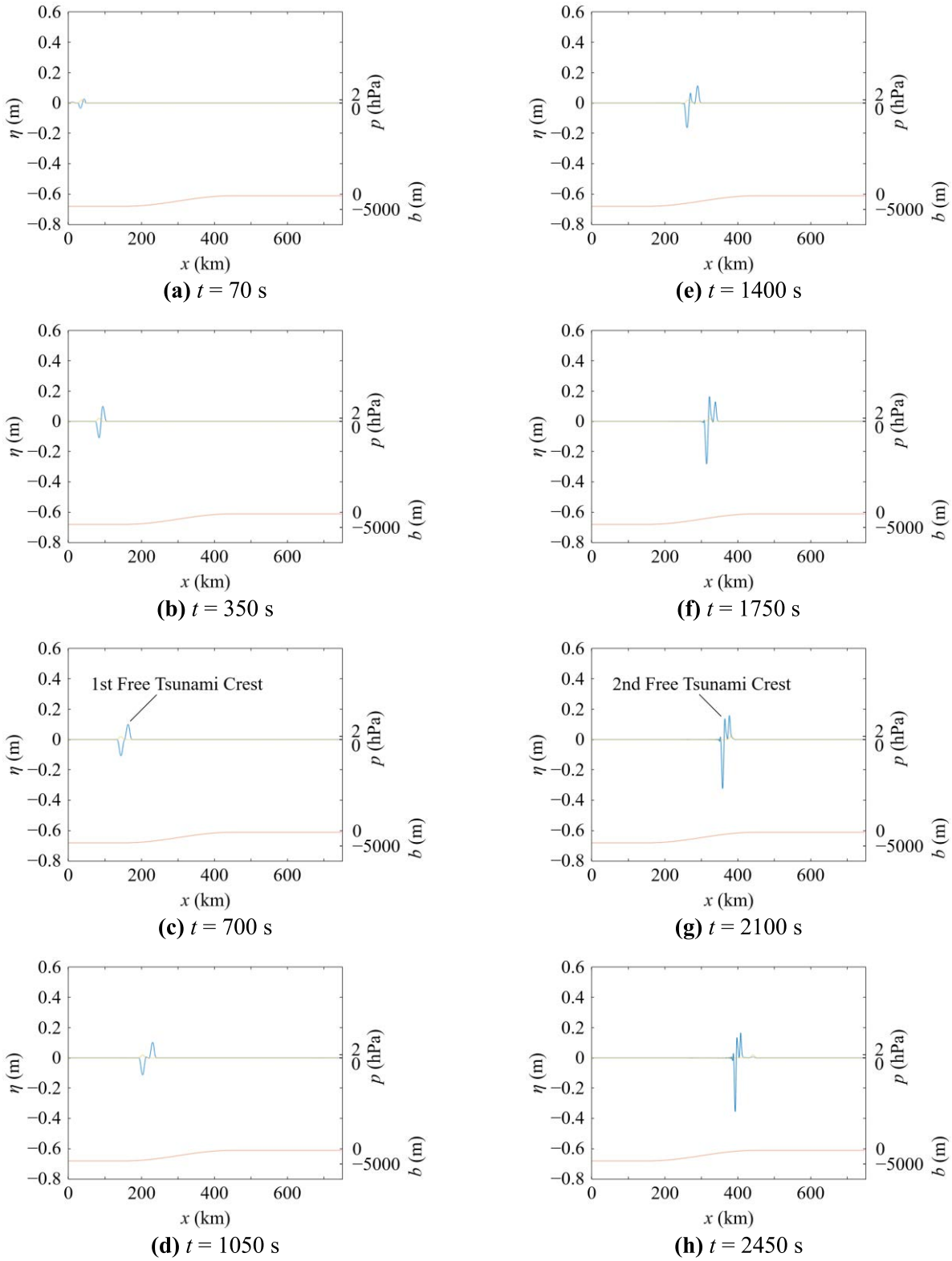

(a) $t = 70$ s **(e)** $t = 1400$ s

(b) $t = 350$ s **(f)** $t = 1750$ s

(c) $t = 700$ s **(g)** $t = 2100$ s

(d) $t = 1050$ s **(h)** $t = 2450$ s

Figure 6. Time variations of the air pressure and water surface profiles in Case 2. The yellow, blue, and orange lines indicate the air pressure p, water surface displacement η, and seabed position b, respectively. The conditions are described in Tables 1 and 2.

3.3. Case 3: $v < c$ in the deepest area and $v > c$ in the shallowest area

In Case 3, an air pressure wave traveled over a seabed including a slope as illustrated in Figure 3, and the calculation conditions are described in Tables 1 and 2. In this case, the approximate value of tsunami speed, c, is $\sqrt{gh_{\text{off}}} \simeq 193$ m/s in the deepest area and $\sqrt{gh_{\text{on}}} = 70$ m/s in the shallowest area. Although $\sqrt{gh_{\text{on}}} = 70$ m/s in both Cases 2 and 3, $\sqrt{gh_{\text{off}}} \simeq 198$ m/s in Case 2, so $\sqrt{gh_{\text{off}}}$ is slightly larger in Case 2 than in Case 3. Conversely, the traveling velocity of the air pressure wave, v, is 170 m/s in Case 3, so $v < c$ in the deepest area and $v > c$ in the shallowest area, as in Case 2. The time variations of both the air pressure and water surface displacement in Case 3 are depicted in Figure 7, with the seabed profile. Over the uphill slope, as shown in Figures 7(d)–7(f), the air pressure wave, which is generating a new tsunami crest, passes the first free tsunami crest. Therefore, the first free tsunami crest and the newly excited tsunami crest partially overlap, and then, in Figure 7(g), this composite wave has been left behind from the air pressure wave. Conversely, as shown in Figure 6(g), two free tsunami crests are separated in Case 2. Based on the difference in the timing of the air pressure wave to pass a free tsunami crest, the maximum water level in Case 3, which exceeds 0.2 m, is larger than that in Case 2. As the overlap degree of the two tsunami crests described above increases, the maximum water level will increase.

Figure 7(h) indicates that the maximum water level has increased because of both the shoaling and the increased overlap degree due to the shorter distance between the leading tsunami peak and the subsequent tsunami peak, which propagates at a larger velocity in a deeper water. In addition, the amplitude of the free tsunami trough further increases because of the soliton disintegration with a tail including several tsunami crests and troughs.

4. Generation and propagation of tsunamis due to air pressure waves over a seabed including slopes

4.1. Case 4: Generation and propagation of tsunamis due to an air pressure wave over a seabed including four slopes

In Case 4, an air pressure wave traveled over a seabed including four slopes as illustrated in Figure 4(a). The calculation conditions are described in Tables 1, 3, and 4. The time variations of both the air pressure and water surface displacement are depicted in Figure 8, with the seabed profile. First, the air pressure wave accompanied by a forced tsunami crest precedes a free tsunami trough in the shallowest area. Then, as depicted in Figures 8(a)–8(c), when the still water depth increases, the effect of the Proudman resonance increases and both a tsunami crest and trough are excited, because the traveling velocity of the air pressure wave, v, is 200 m/s and the resonance effect is maximized when the still water depth h is around 4080 m. It should be noted that the amplitude of the tsunami crest is larger than that of the tsunami trough because only the free component of the tsunami trough has been left behind the air pressure wave over the shallower area. Figure 8(d) indicates that at the valley or trench, the approximate tsunami speed c is larger than the traveling speed of the air pressure wave, v, so the tsunami crest precedes the air pressure wave accompanied by the tsunami trough. In Figure 8(e), a free tsunami trough also precedes the air pressure wave accompanied by a tsunami trough with a decreased amplitude. In Figures 8(f) and 8(g), another tsunami crest and trough are generated and amplified based on larger

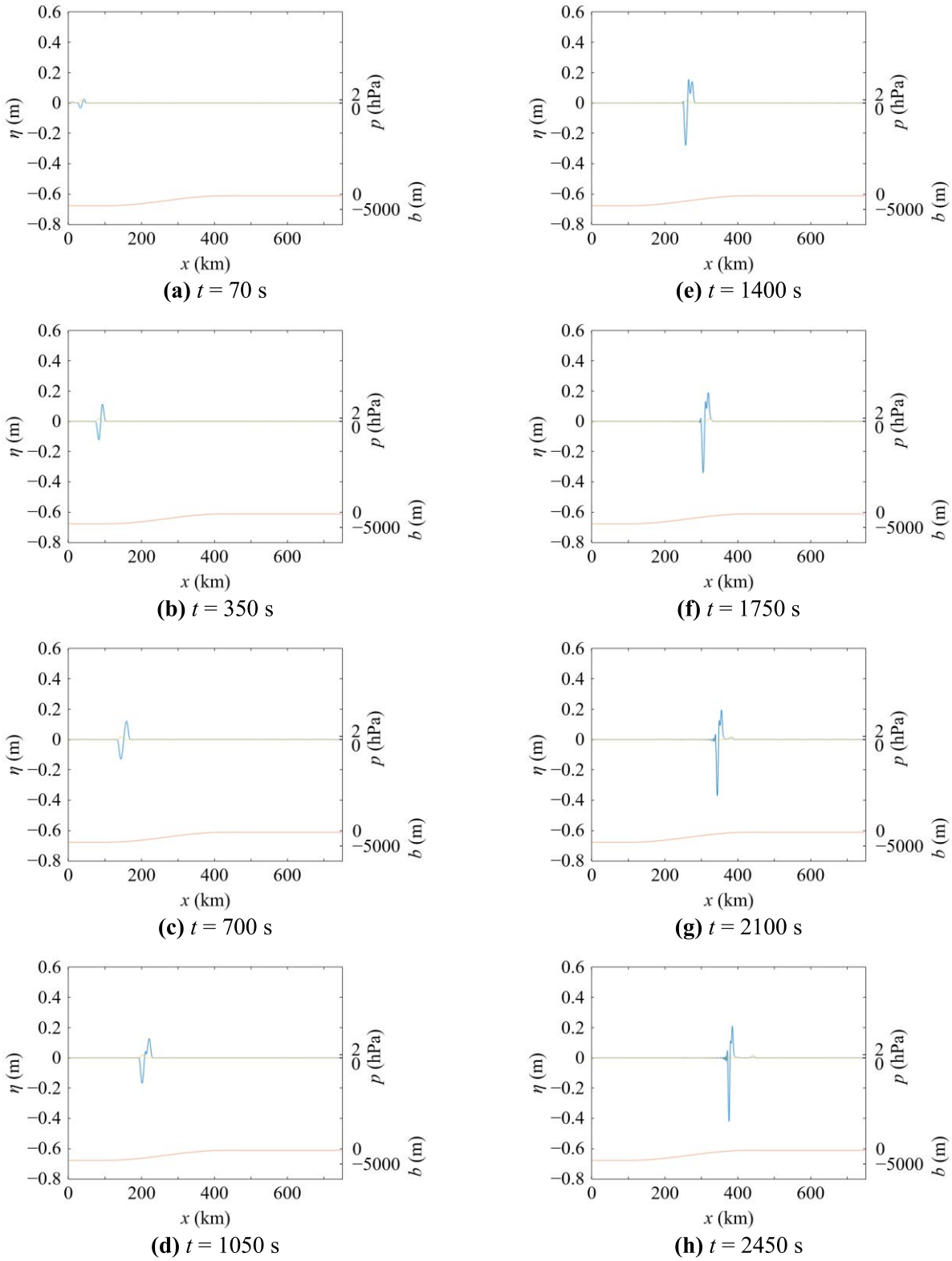

Figure 7. Time variations of the air pressure and water surface profiles in Case 3. The yellow, blue, and orange lines indicate the air pressure p, water surface displacement η, and seabed position b, respectively. The conditions are described in Tables 1 and 2.

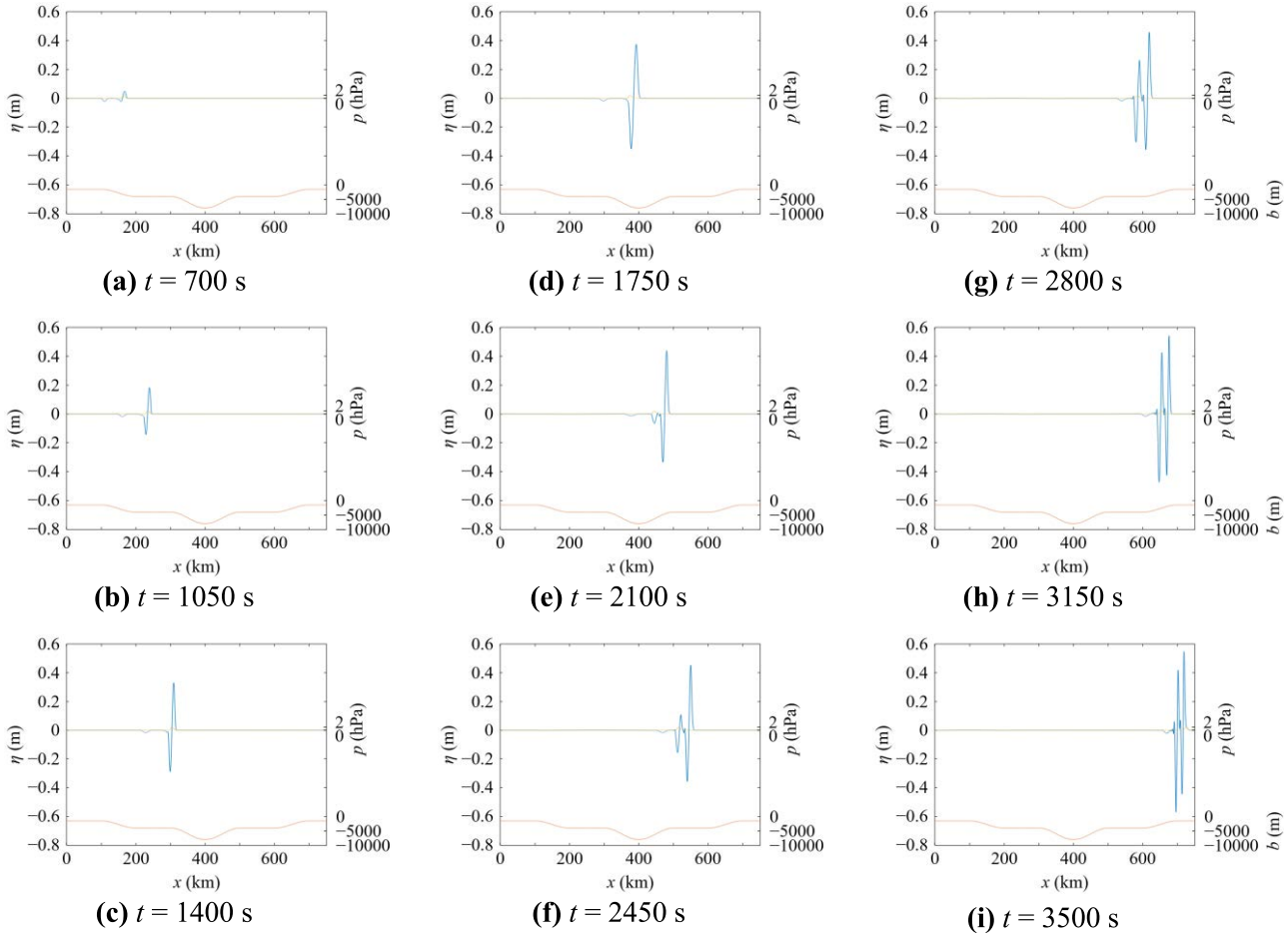

Figure 8. Time variations of the air pressure and water surface profiles in Case 4. The yellow, blue, and orange lines indicate the air pressure p, water surface displacement η, and seabed position b, respectively. The conditions are described in Tables 1, 3, and 4.

Proudman resonance effect due to the decrease in still water depth. Thus, multiple free tsunami crests and troughs are excited over seabed slopes, even though just one air pressure wave travels.

It should be noted that the intervals of the free tsunamis decrease and the total length of the free wave group becomes shorter as the still water depth decreases. There are two reasons for this as follows:

(1) The propagating velocities of preceding free tsunami crests and troughs decrease, so subsequent free tsunamis traveling in deeper water approach the preceding free tsunamis.

(2) Tsunamis that are just excited by air pressure waves approach the preceding free tsunamis with a propagating velocity slower than the traveling speed of the air pressure waves.

4.2. Case 5: Generation and propagation of tsunamis due to three air pressure waves over a seabed including four slopes

In Case 5, three air pressure waves traveled over a seabed including four slopes as illustrated in Figure

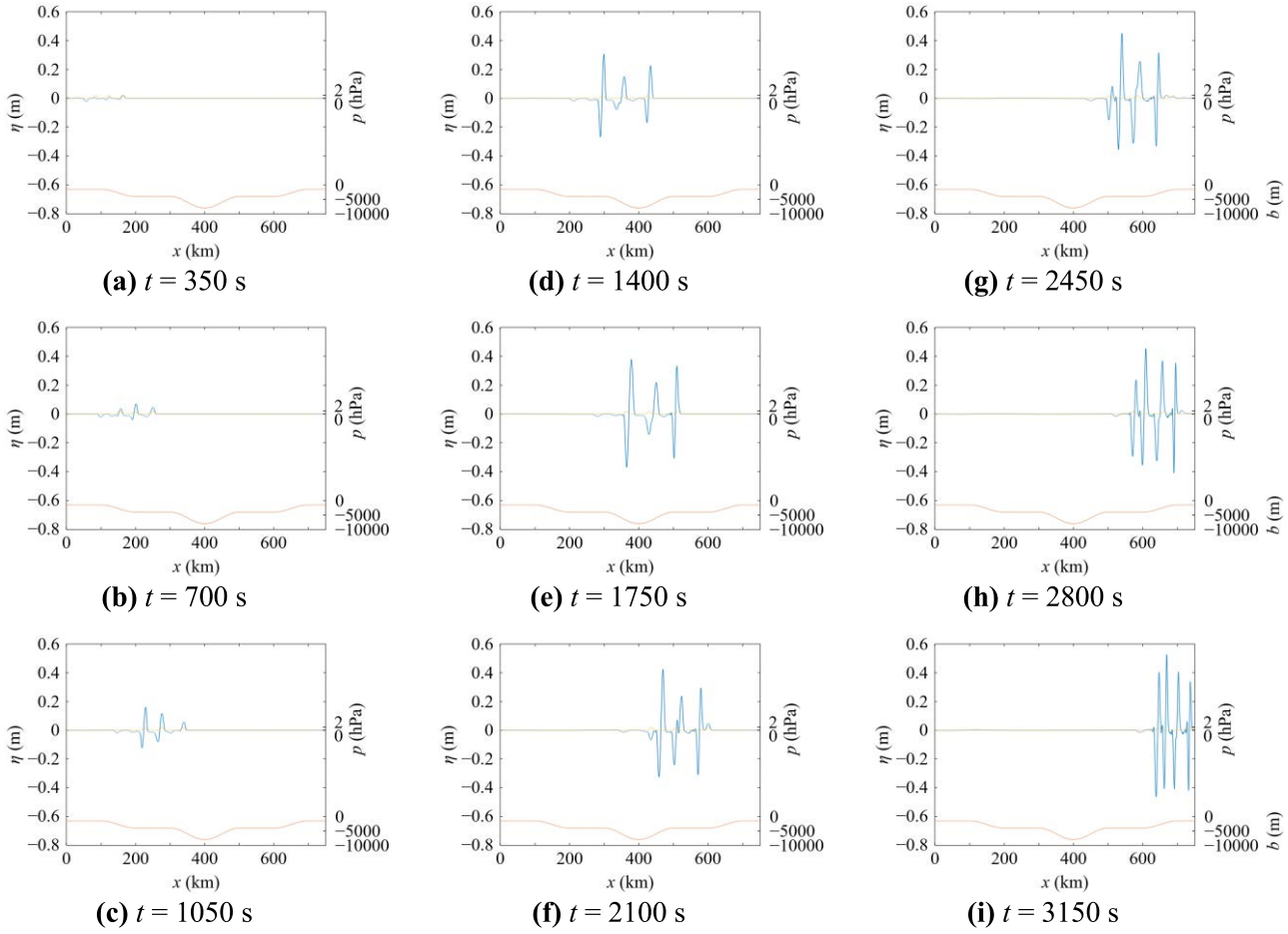

Figure 9. Time variations of the air pressure and water surface profiles in Case 5. The yellow, blue, and orange lines indicate the air pressure p, water surface displacement η, and seabed position b, respectively. The conditions are described in Tables 1, 3, and 4.

4(a). The calculation conditions are described in Tables 1, 3, and 4. Although the traveling speeds of the air pressure waves are different and the Proudman resonance effect becomes greater in different sea areas [20], the traveling speeds of the air pressure waves, v_n (n = 1–3), are larger than the approximate propagating velocity of a free tsunami, c, in the shallowest area, while $v_n < c$ in the deepest area. The time variations of both the air pressure and water surface displacement are depicted in Figure 9, with the seabed profile. Comparing Figures 9(d) and 9(i), although the latter shows one more significant free tsunami crest and trough than the former, the total length of the latter free wave group is shorter than that of the former, because the subsequent tsunamis approach the preceding tsunamis, as described above for Case 4.

4.3. Case 6: Generation and propagation of tsunamis due to three air pressure waves over a seabed including three slopes

In Case 6, three air pressure waves traveled over a seabed including three slopes as illustrated in Figure 4(b). The calculation conditions are described in Tables 1, 3, and 4. As in Case 5, $v_n > c$ in the shallowest area, while $v_n < c$ in the deepest area. The time variations of both the air pressure and water surface

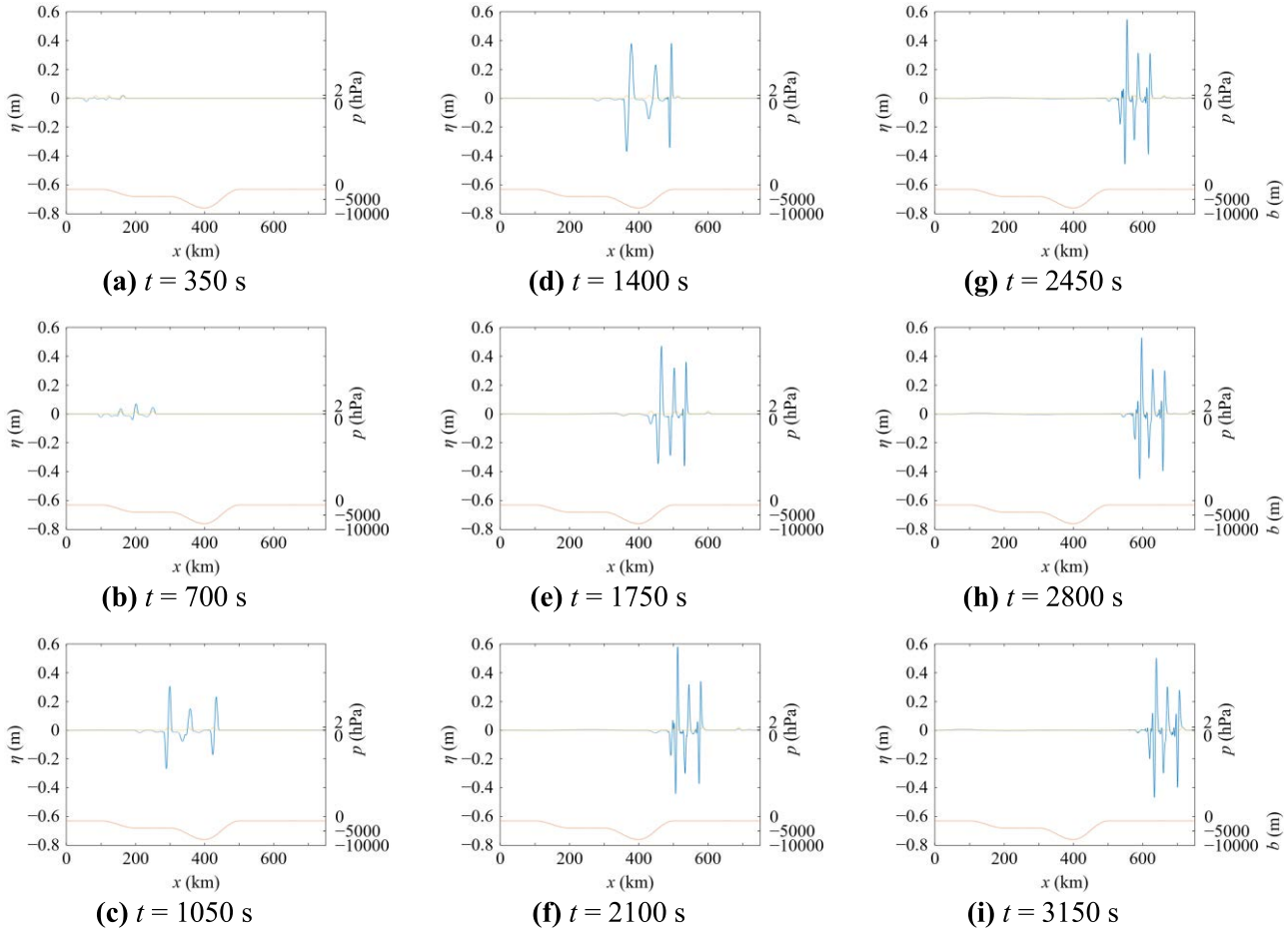

Figure 10. Time variations of the air pressure and water surface profiles in Case 6. The yellow, blue, and orange lines indicate the air pressure p, water surface displacement η, and seabed position b, respectively. The conditions are described in Tables 1, 3, and 4.

displacement are depicted in Figure 10, with the seabed profile. In Figure 9(i) for Case 5, the number of both the tsunami crests and troughs with an amplitude over 0.2 m is four, while that is three in Figure 10(i). Thus, the numbers of free tsunami crests and troughs with a larger amplitude depend on the number of seabed slopes, as well as the number of air pressure waves that excite tsunamis.

5. Conclusions

Numerical simulations were generated using the nonlinear shallow water model on velocity potential to study the excitation and propagation of tsunamis due to steady air pressure waves over typical seabed topographies. We set the conditions by considering the magnitude relationship between the traveling speed of air pressure waves, v, and the approximate propagating velocity of free tsunamis, c.

First, we assumed that an air pressure wave traveled over a seabed including an upslope. When $v > c$ in the whole region, the air pressure wave accompanied by a forced tsunami crest preceded the generated free tsunami trough over the horizontal seabed. Thereafter, over the upslope seabed, the air pressure wave with the forced tsunami crest gradually formed a free tsunami crest with a larger

wavelength, and then this free tsunami crest was left behind the air pressure wave.

When $v < c$ in the deeper area and $v > c$ in the shallower area, the air pressure wave accompanied by a forced tsunami trough was preceded by the generated free tsunami crest over the horizontal seabed. After that, over the upslope seabed, the air pressure wave with the forced tsunami trough generated a new tsunami crest. As the overlap degree of the new tsunami crest and the preceding free tsunami crest was increased, the maximum water level increased. Conversely, the forced tsunami trough brought by the air pressure wave was amplified based on the larger Proudman resonance effect. Furthermore, the preceding free tsunami crest was amplified both by shoaling and by being passed by the air pressure wave.

Second, we assumed that air pressure waves traveled over a seabed including multiple slopes, where $v < c$ in the deepest area and $v > c$ in the shallowest area. Multiple significant free tsunami crests and troughs were excited by just one air pressure wave because of the multiple slopes. The numbers of the significant tsunami crests and troughs depended on the number of the seabed slopes, as well as the number of the air pressure waves that excited tsunamis.

Funding

This work was supported by JSPS KAKENHI Grant Number JP22H01136, the Research Institute for Mathematical Sciences, an International Joint Usage/Research Center located in Kyoto University, and the Collaborative Research Program of Research Institute for Applied Mechanics, Kyushu University.

Conflicts of Interest

The authors declare no conflict of interest.

References

1. Japan Meteorological Agency Earthquake Volcano Department. On the tide level change due to the large eruption of Hunga Tonga–Hunga Ha`apai volcano near the Tonga Islands around 13:00 on January 15, 2022. *Japan Meteorological Agency Press Release* 2022, *11* (in Japanese). https://www.jma.go.jp/jma/press/2201/16a/kaisetsu202201160200.pdf (accessed on March 14, 2024).
2. Proudman, J. The effects on the sea of changes in air pressure. *Geophysical Journal International* 1929, *2(s4)*, 197–209. doi: 10.1111/j.1365-246X.1929.tb05408.x.
3. Kakinuma, T. Long-wave generation due to air pressure variation and harbor oscillation in harbors of various shapes and countermeasures against meteotsunamis. In *Natural Hazards—Risk, Exposure, Response, and Resilience*; Tiefenbacher, J.P., Ed.; IntechOpen: London, UK, 2019; pp. 81–109. doi: 10.5772/ intechopen.85483.
4. Symons, G.J., Ed. *The eruption of Krakatoa, and subsequent phenomena, Report of the Krakatoa Committee of the Royal Society*; Trübner and Co.: London, 1888; 494p.
5. Imamura, A. Observation of Krakatau explosion tsunami in Japan: Earthquake Chat (10). *Earthquake* 1934, *1(6)*, 158–160 (in Japanese).

6. Verbeek, R.D.M. *Krakatau*; Government Press: Batavia, 1885; 495p.
7. Harkrider, D.; Press, F. The Krakatoa air-sea waves: an example of pulse propagation in coupled systems. *Geophysical Journal International* 1967, *13*, 149–159. doi: 10.1111/j.1365-246X.1967.tb02150.x.
8. Garrett, C.J.R. A theory of the Krakatoa tide gauge disturbances. *Tellus* 1970, *22(1)*, 43–52. doi: 10.1111/j.2153-3490.1970.tb01935.x.
9. Yokoyama, I. A geophysical interpretation of the 1883 Krakatau eruption. *Journal of Volcanology and Geothermal Research* 1981, *9(4)*, 359–378. doi: 10.1016/0377-0273(81)90044-5.
10. Yokoyama, I. A scenario of the 1883 Krakatau tsunami. *Journal of Volcanology and Geothermal Research* 1987, *34(1–2)*, 123–132. doi: 10.1016/0377-0273(87)90097-7.
11. Pelinovsky, E.; Choi, B.H.; Stromkov, A.; Didenkulova, I.; Kim, H.-S. Analysis of tide-gauge records of the 1883 Krakatau Tsunami, In *Tsunamis. Advances in Natural and Technological Hazards Research*; Satake, K., Ed.; Springer: Dordrecht, 2005; p. 23. doi: 10.1007/1-4020-3331-1_4.
12. Kobayashi, T.; Kakinuma, T. Tsunamis propagated by airwaves generated by explosive volcanic eruptions: the 1883 Krakatau and the 1956 Bezymianny eruptions. In *Proceedings of the International Meeting on Eruptive History and Informatics 2021-2*, Fukuoka, March 5–6, 2022; pp. 93–105 (in Japanese).
13. Soloviev, S.L. Basic data of tsunamis in the Pacific coast of USSR, 1937–1976, In *A Study of Tsunamis in the Open Sea*; Academii Nauk: Moscow, 1978; pp. 61–136 (in Russian).
14. Tanioka, Y.; Yamanaka, Y.; Nakagaki, T. Characteristics of the deep sea tsunami excited offshore Japan due to the air wave from the 2022 Tonga eruption. *Earth, Planets and Space* 2022, *74(61)*. doi: 10.1186/s40623-022-01614-5.
15. Kubota, T.; Saito, T.; Nishida, K. Global fast-traveling tsunamis driven by atmospheric Lamb waves on the 2022 Tonga eruption. *Science* 2022, eabo4364. doi: 10.1126/science.abo4364.
16. Watanabe, S.; Hamilton, K.; Sakazaki, T.; Nakano, M. First detection of the Pekeris internal global atmospheric resonance: Evidence from the 2022 Tonga eruption and from global reanalysis data. *J. Atmos. Sci.* 2022, 3027–3043. doi: 10.1175/JAS-D-22-0078.1.
17. Suzuki, T.; Nakano, M.; Watanabe, S.; Tatebe, H.; Takano, Y. Mechanism of a meteorological tsunami reaching the Japanese coast caused by Lamb and Pekeris waves generated by the 2022 Tonga eruption. *Ocean Modelling* 2023, *181*, 102153. doi: 10.1016/j.ocemod.2022.102153.
18. Kakinuma, T. Tsunamis generated and amplified by atmospheric pressure waves due to an eruption over seabed topography. *Geosciences* 2022, *12(6)*, 232. doi: 10.3390/geosciences12060232.
19. Kakinuma, T. Numerical simulation of surface and internal wave excitation due to an air pressure wave. *Geology, Earth and Marine Sciences* 2023, *5(3)*. doi: 10.31038/GEMS.2023533.
20. Yamashita, K.; Kakinuma, T. Interpretation of global tsunami height distribution due to the 2022 Hunga Tonga–Hunga Ha`apai volcanic eruption. *Preprint available at Research Square* 2022. doi: 10.21203/rs.3.rs-1761920/v1.